Power Optimization and Control in Wind Energy Conversion Systems Using Extremum Seeking

Azad Ghaffari, Miroslav Krstić, *Fellow, IEEE*, and Sridhar Seshagiri

***Abstract*— Power optimization and control for grid-coupled wind energy conversion systems (WECS) has been extensively studied for variable speed wind turbines. However, existing methods widely use model-based power optimization algorithms in the outer loop along with linear control techniques in the inner loop. The transient performance of this combination is dependent on the system's operating point, especially under fast varying wind regimes. We employ extremum seeking (ES) in the outer loop, which is a nonmodel-based optimization approach, to perform maximum power point tracking, i.e., extract maximum power from WECS in their subrated power region. Since the convergence rate of the ES design may be limited by the speed of the system dynamics, we also design a nonlinear controller, based on the field-oriented control concept and feedback linearization, that yields improvement in convergence rate by two orders of magnitude. The outer ES loop tunes the turbine speed to maximize power capture for all wind speeds within the subrated power operating conditions. The inner-loop nonlinear control maintains fast transient response through a matrix converter, by regulating the electrical frequency and voltage amplitude of the stator of the (squirrel-cage) induction generator. Simulation results are presented to show the effectiveness of the proposed design.**

***Index Terms*— Adaptive systems, nonlinear control systems, power control, wind power generation.**

I. Introduction

A VARIABLE speed wind turbine (WT) generates power in two different regions, subrated power region and rated power region. In the subrated power region, the maximum achievable turbine power is a function of the turbine speed at any given wind velocity. To achieve maximum power point tracking (MPPT), i.e., extract maximum power, an optimization algorithm is needed [5], [8], [13], [15], [17], [20], [26]–[28], and is often used in conjunction with a controller that guarantees other closed-loop desired performance specifications. In this paper, we focus on the optimization and control of a wind energy conversion system (WECS) composed of a WT, a squirrel-cage induction generator (IG), and a matrix converter (MC). The MC, which is a replacement for the conventional rectifier–inverter combination (ac–dc–ac), features no energy storage components, has bidirectional power flow capability and controllable input power factor [37]. It connects the IG to the power grid, and along with the presented control/optimization design, steers the WT to its maximum power point (MPP) by controlling the electrical frequency and voltage amplitude of the stator of IG, which in turn leads to a variation in the turbine speed. It also assists in voltage regulation or power factor correction by controlling the reactive power transfer to the grid.

A design for a system similar to the one we consider here has been presented in [5], and is based on a speed-sensoreless power signal feedback (PSF) algorithm. The speed-sensoreless PSF algorithm uses lookup table values that are dependent on the system model and parameter values. In addition, accuracy of the method depends on the accuracy and resolution of the data obtained for the lookup table. Furthermore, the control design employs Jacobian linearization, and uncertainty in the system dynamics and/or variations in the working conditions cause the system to move away from its MPP. Another method based on fuzzy logic principles and four-leg-improved MC model, used for performance enhancement and efficiency optimization, is presented in [20]. Model-dependent designs have the drawback that the optimization algorithm and controller need to be redesigned carefully for each WECS. To overcome these difficulties, we present an extremum seeking (ES) algorithm, which is: 1) nonmodel based and 2) with easily tunable design parameters [2], [3], [19], [30]–[33]. Furthermore, ES shows promising results for a wide variety of applications [6], [10], [11], [16], [23], [34]. ES designs for MPPT of WECS are also presented in [8], [17], and [26], but differ from the design in this paper in several respects, including assumptions on the system model, transient performance, and performance robustness.

With the exception of [5], none of the previous works on the power extraction have focused on the transient performance, and the model in [5], unlike ours, is based on linearization and is highly model dependent. While the ES design we present alleviates this problem, a requirement for the design is that its dynamics be slower than that of the WECS. While the WECS system is stable by itself, its linearization has slow poles, which therefore limits the convergence rate for the ES algorithm. To improve the transient response, we propose an inner-loop IG control based on field-oriented control (FOC), the elements of which can be found in [21] and [24]. For the ES design, the turbine speed is considered as the variable

Manuscript received August 2, 2013; revised November 11, 2013 and January 15, 2014; accepted January 21, 2014. Manuscript received in final form January 25, 2014. Date of publication February 19, 2014; date of current version July 24, 2014. Recommended by Associate Editor A. G. Aghdam.

A. Ghaffari and M. Krstić are with the Department of Mechanical and Aerospace Engineering, University of California at San Diego, La Jolla, CA 92093-0411 USA (e-mail: aghaffari@ucsd.edu; krstic@ucsd.edu).

S. Seshagiri is with the Department of Electrical and Computer Engineering, San Diego State University, San Diego, CA 92182-1309 USA (e-mail: seshagir@engineering.sdsu.edu).

Color versions of one or more of the figures in this paper are available online at http://ieeexplore.ieee.org.

Digital Object Identifier 10.1109/TCST.2014.2303112

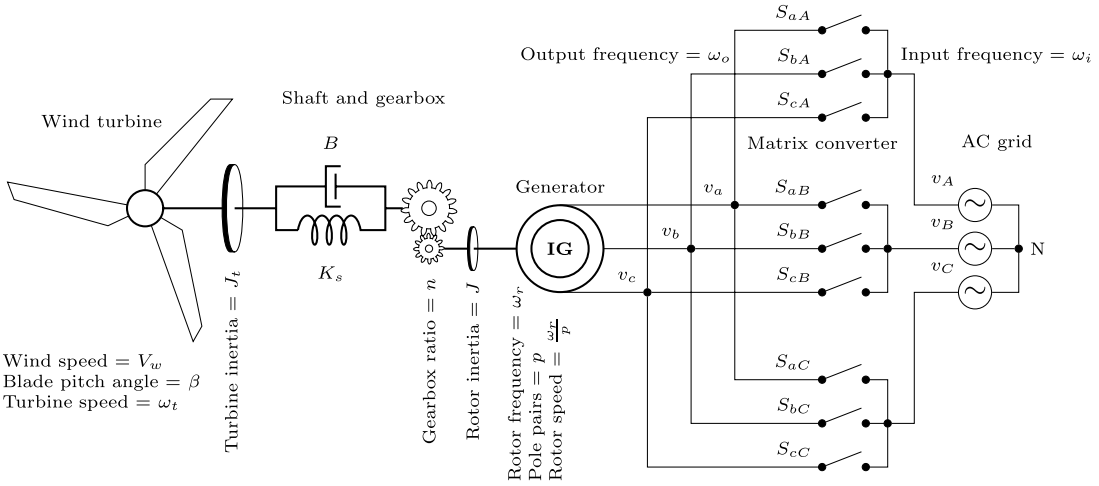

Fig. 1. WECS including WT, gear box, IG, and MC.

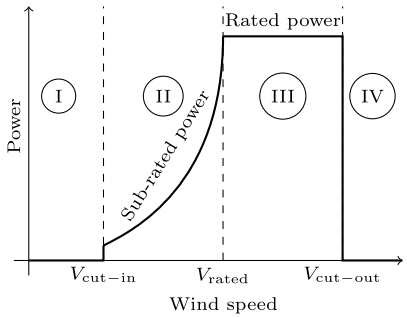

Fig. 2. Typical power curve of WT including four operating regions.

parameter to tune MPP. The turbine power is the cost function for the ES algorithm, and electrical frequency and voltage amplitude of the stator of IG are controlled through the MC to reach desired closed-loop performance. As a result of including the inner loop, the overall design has faster response time, and furthermore magnetic saturation of the IG is avoided. In comparison with model-based designs, ES better handles model uncertainty in the turbine power map, resulting in improved power extraction. To the best of our knowledge, this is the first work in the literature that combines the MPPT with nonlinear control design that has good performance robustness to uncertainty, and faster transient performance, allowing for power tracking under rapidly varying wind conditions.

The rest of this paper is organized as follows. An introduction to modeling of the WECS with concentration on the squirrel-cage IG dynamics in stationary reference frame and the MC is discussed in Section II. Our nonlinear controller design is discussed in Section III, and the ES algorithm in Section IV. Simulation results to verify the effectiveness of the proposed scheme are presented in Section V, and our conclusion is presented in Section VI.

II. Wind Energy Conversion System

A schematic diagram of a WECS including WT, IG, and MC is shown in Fig. 1. WTs work in four different regions, as shown in Fig. 2. In Region I, the wind speed is too low for the turbine to generate power. Region II, also called the subrated power region, lies between the cut-in speed and rated speed. Here, the generator operates at below rated power. The theoretical shape of this curve reflects the basic law of power production, where power is proportional to the cube of the wind speed. In Region III, the power output is limited by the turbine; this occurs when the wind is sufficient for the turbine to reach its rated output power. Region IV is the period of stronger winds, where the power in the wind is so great that it could be detrimental to the turbine, so the turbine shuts down [14].

The wind power available on the blade impact area is defined as

$$P_w = \frac{1}{2}\rho A V_w^3, \quad A = \pi R^2 \tag{1}$$

where R is the blade length and V_w is wind speed. For Region II MPPT, assuming zero blade pitch angle, the turbine power is related to the wind power as

$$P_t = \omega_t T_t = C_p(V_w, \omega_t) P_w \tag{2}$$

where T_t is the rotor torque, ω_t is the turbine speed, and C_p is the nondimensional power coefficient, which is a measure of the ratio of the turbine power to the wind power. The power coefficient is a function of wind and turbine speed. The theoretical limit for C_p is 0.59 according to Betz's law, but its practical range of variation is 0.2–0.4 [20]. The power coefficient has been approximated numerically in several references, e.g., [1] and [29]. For simulation purposes, we select one of the most common equations used for power coefficient as follows:

$$C_p(V_w, \omega_t) = 0.73 \frac{151 \frac{V_w}{R\omega_t} - 13.635}{\exp\left(\frac{V_w}{R\omega_t} - 0.003\right)}. \tag{3}$$

Power coefficient (3) depends on the turbine speed, which can be used for power control and optimization. The MPPT algorithm in subrated power region should be able to govern the WT to its MPP regardless of the variations of the wind speed. As shown in Fig. 3, the maximum value of the power coefficient happens at different turbine speeds when wind speed is varying, but the maximum value stays at the same level of C_p^*.

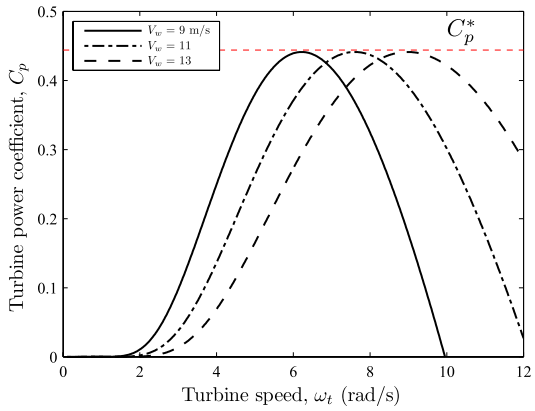

Fig. 3. Variation of turbine power coefficient versus turbine speed for different wind speeds where $\beta = 0$. The maximum value of the power coefficient is C_p^*.

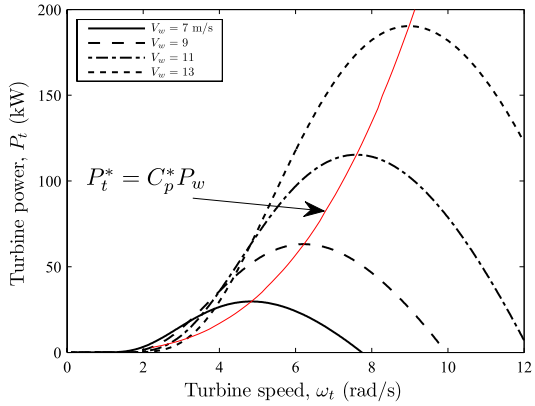

Fig. 4. Variation of the turbine power versus turbine speed for different wind speeds where $\beta = 0$. The MPP moves on $C_p^* P_w$ curve, which shows the characteristic of the subrated region of WECS.

From (1)–(3), and considering the fact that the blade pitch angle is zero, we have

$$P_t(V_w, \omega_t) = 55.115 \rho A \frac{\frac{V_w}{R\omega_t} - 0.09}{\exp\left(\frac{V_w}{R\omega_t} - 0.003\right)} V_w^3 \tag{4}$$

which shows that the power captured by the WT is defined by the wind speed, V_w, and the turbine speed, ω_t. However, the wind speed is a disturbance input and we can manipulate the turbine speed to govern the turbine power to its MPP in subrated region. The variation of turbine power versus turbine speed is shown in Fig. 4 for different wind speeds. From (4) and as shown in Fig. 4 under a constant wind speed, the relevant power curve has a unique MPP, which is defined by a specific turbine speed. In addition, the MPP moves on a third-order curve, which defines the maximum power captured by the WT.

As shown in Fig. 1, the WT shaft is modeled as a spring damper. The dynamic equations of the turbine, the shaft, and the gearbox are

$$\frac{\mathrm{d}}{\mathrm{d}t}\tilde{\theta} = \omega_t - \frac{\omega_r}{pn}, \quad \tilde{\theta} = \theta_t - \frac{\theta_r}{pn} \tag{5}$$

$$\frac{\mathrm{d}}{\mathrm{d}t}\omega_t = \frac{1}{J_t}\left(-T_t - T_L\right), \quad T_t = \frac{P_t(V_w, \omega_t)}{\omega_t} \tag{6}$$

where ω_r is the angular electrical frequency of the rotor of IG, θ_t is WT angular position, θ_r is the electrical angle of the rotor of IG, p is the number of pole pairs of the IG, n is the gearbox ratio, T_t is the turbine torque generated by the turbine power, and T_L is the load torque created by the spring-damper model of the shaft

$$T_L = K_s\tilde{\theta} + B\left(\omega_t - \frac{\omega_r}{pn}\right) \tag{7}$$

where K_s is the stiffness coefficient of the spring and B is the damping ratio. The generator rotor angular speed equals ω_r/p. The numerical values of the parameters are given in Table I (see Appendix).

Squirrel-cage IGs are relatively inexpensive, robust, and require a little maintenance. When operated using vector control techniques, fast dynamic response, and accurate torque control is obtained [9]. From [18], the (α, β) model equations for the squirrel-cage IG are as follows:

$$\frac{\mathrm{d}}{\mathrm{d}t}i_\alpha = -a_0 i_\alpha + a_1\lambda_\alpha + a_2\omega_r\lambda_\beta + \frac{\upsilon_\alpha}{\sigma L_s} \tag{8}$$

$$\frac{\mathrm{d}}{\mathrm{d}t}i_\beta = -a_0 i_\beta - a_2\omega_r\lambda_\alpha + a_1\lambda_\beta + \frac{\upsilon_\beta}{\sigma L_s} \tag{9}$$

$$\frac{\mathrm{d}}{\mathrm{d}t}\lambda_\alpha = a_3 i_\alpha - a_4\lambda_\alpha - \omega_r\lambda_\beta \tag{10}$$

$$\frac{\mathrm{d}}{\mathrm{d}t}\lambda_\beta = a_3 i_\beta - a_4\lambda_\beta + \omega_r\lambda_\alpha \tag{11}$$

$$\frac{\mathrm{d}}{\mathrm{d}t}\omega_r = \frac{p}{J}\left(T_e - \frac{T_L}{n}\right) \tag{12}$$

where i_α and i_β are stator currents, λ_α and λ_β are rotor flux linkages, υ_α and υ_β are stator voltages, and the electromagnetic torque generated by the IG is

$$T_e = \frac{3}{2}p\frac{L_m}{L_r}\left(i_\beta\lambda_\alpha - i_\alpha\lambda_\beta\right) \tag{13}$$

where L_m is the mutual inductance, $L_s = L_{ls} + L_m$ is stator inductance, $L_r = L_{lr} + L_m$ is rotor inductance, and $\sigma = 1 - L_m^2/(L_r L_s)$. The numerical values of the parameters are defined in the Appendix.

Remark 1: Since MPPT in subrated power region is the main focus of this paper and, as shown in Fig. 2, the turbine power curve stays above zero, then (2) implies a nonzero turbine speed, $\omega_t \neq 0$, for $V_{\text{cut-in}} < V_w < V_{\text{rated}}$, which also leads to $\lambda_\alpha^2 + \lambda_\beta^2 \neq 0$.

As shown in Fig. 1, the generator is connected to the ac grid through an MC, which includes nine bidirectional switches operating in 27 different combinations. MCs provide bidirectional power flow, sinusoidal input/output currents, and controllable input power factor. Due to the absence of components with significant wearout characteristics (such as electrolytic capacitors), MC can potentially be very robust and reliable. The amount of space saved by an MC, when compared with a conventional back-to-back converter, has been estimated as a factor of three. Therefore, due to its small size, in some applications, the MC can be embedded in the machine.

Furthermore, there is no intrinsic limitation to the power rating of an MC [9]. Therefore, we use MCs instead of conventional back-to-back converters. The model for MCs that

we use is based on [4], [12], and [35]. The input phase voltage of MC, $v_i = [v_A \;\; v_B \;\; v_C]^T$, which is connected to the ac grid, is given by

$$v_i = V_{\text{im}} \left[\cos\theta_i \;\; \cos\left(\theta_i - \frac{2\pi}{3}\right) \;\; \cos\left(\theta_i + \frac{2\pi}{3}\right) \right]^T \quad (14)$$

where V_{im} is the peak value of the input voltage amplitude and

$$\theta_i = \int_0^t \omega_i \mathrm{d}\tau \quad (15)$$

is the input electrical angle, where $\omega_i = 2\pi f_i$ is the input electrical frequency of the MC. In this case, due to the inductive nature of the IG, the output phase current can be assumed sinusoidal, and hence given by

$$i_o = I_{\text{om}} \begin{bmatrix} \cos(\theta_o + \phi_o) \\ \cos\left(\theta_o + \phi_o - \frac{2\pi}{3}\right) \\ \cos\left(\theta_o + \phi_o + \frac{2\pi}{3}\right) \end{bmatrix} \quad (16)$$

where I_{om} is the peak value of the output current amplitude, ϕ_o is the load displacement angle at the output frequency $\omega_o = 2\pi f_o$, and

$$\theta_o = \int_0^t \omega_o \mathrm{d}\tau \quad (17)$$

is the output electrical angle.

Output voltage is $v_o = [v_a \;\; v_b \;\; v_c]^T$. It is the job of the MC to create local-averaged sinusoidal output phase voltage (the stator voltage of IG) and input phase current (the ac grid current)

$$\bar{v}_o = V_{\text{om}} \left[\cos\theta_o \;\; \cos\left(\theta_o + \frac{2\pi}{3}\right) \;\; \cos\left(\theta_o + \frac{2\pi}{3}\right) \right]^T \quad (18)$$

$$\bar{i}_i = I_{\text{im}} \begin{bmatrix} \cos(\theta_i + \phi_i) \\ \cos\left(\theta_i + \phi_i - \frac{2\pi}{3}\right) \\ \cos\left(\theta_i + \phi_i + \frac{2\pi}{3}\right) \end{bmatrix} \quad (19)$$

where ϕ_i is the input displacement angle, which controls the power factor at the grid connection. Output electrical frequency, ω_o, and voltage amplitude, V_{om}, are actuated through MC to achieve desired closed-loop performance. More details about MC modeling can be found in [4], [35], and [12].

We are interested in finding modulation matrices such that

$$\bar{v}_o = S v_i \quad (20)$$

$$\bar{i}_i = S^T i_o. \quad (21)$$

The solutions to the modulation problem should satisfy: 1) restrictions on the duty cycle of the MC switches that prevent short circuit of the input sources and open circuit of the inductive load; 2) sinusoidal output voltages with controllable frequency and magnitude; 3) sinusoidal input currents; and 4) desired input displacement power factor [4]. There are two basic solutions, which satisfy 1)–3)

$$S_1 = \frac{1}{3} \begin{bmatrix} 1 & 1 & 1 \\ 1 & 1 & 1 \\ 1 & 1 & 1 \end{bmatrix} + \frac{2}{3} m T_1 \quad (22)$$

$$S_2 = \frac{1}{3} \begin{bmatrix} 1 & 1 & 1 \\ 1 & 1 & 1 \\ 1 & 1 & 1 \end{bmatrix} + \frac{2}{3} m T_2 \quad (23)$$

where

$$m = \frac{V_{\text{om}}}{V_{\text{im}}}, \qquad 0 \le m \le \frac{\sqrt{3}}{2} \quad (24)$$

is the MC output-to-input voltage gain and

$$T_1 = \begin{bmatrix} \cos\theta_1 & \cos\left(\theta_1 - \frac{2\pi}{3}\right) & \cos\left(\theta_1 + \frac{2\pi}{3}\right) \\ \cos\left(\theta_1 + \frac{2\pi}{3}\right) & \cos\theta_1 & \cos\left(\theta_1 - \frac{2\pi}{3}\right) \\ \cos\left(\theta_1 - \frac{2\pi}{3}\right) & \cos\left(\theta_1 + \frac{2\pi}{3}\right) & \cos\theta_1 \end{bmatrix} \quad (25)$$

$$T_2 = \begin{bmatrix} \cos\theta_2 & \cos\left(\theta_2 - \frac{2\pi}{3}\right) & \cos\left(\theta_2 + \frac{2\pi}{3}\right) \\ \cos\left(\theta_2 - \frac{2\pi}{3}\right) & \cos\left(\theta_2 + \frac{2\pi}{3}\right) & \cos\theta_2 \\ \cos\left(\theta_2 + \frac{2\pi}{3}\right) & \cos\theta_2 & \cos\left(\theta_2 - \frac{2\pi}{3}\right) \end{bmatrix} \quad (26)$$

where $\theta_1 = \theta_i - \theta_o$ and $\theta_2 = \theta_i + \theta_o$. The solution in (22) yields $\phi_i = \phi_o$, giving the same phase displacement at the input and output ports, whereas the solution in (23) yields $\phi_i = -\phi_o$, giving reversed phase displacement. Combining the two solutions provides the means for input displacement factor control [4], [35]

$$S = cS_1 + (1-c)S_2, \quad 0 \le c \le 1 \quad (27)$$

where c controls the power factor at the grid side. Reactive power control is not the focus of this paper, so we simply set $c = 0.5$ to obtain unity displacement power factor at the MC input terminals. However, this does not result in a unity displacement power factor at input source terminals.

Considering zero losses in MC, the input and output powers are equal and related as follows:

$$P_i \equiv \frac{3}{2} V_{\text{im}} I_{\text{im}} \cos\phi_i \quad (28)$$

$$P_o \equiv \frac{3}{2} V_{\text{om}} I_{\text{om}} \cos\phi_o. \quad (29)$$

From (24) and equating (28) and (29), we have

$$I_{\text{im}} = m \frac{\cos\phi_o}{\cos\phi_i} I_{\text{om}}. \quad (30)$$

We perform our design in the (α, β) framework. We need to transform the output voltage to the stationary frame and calculate the supplied current to the grid based on the stator current. The local-averaged voltage of the stator is $\bar{v}_o$. Three-phase variables are transformed to two-phase stationary frame [25]

$$\begin{bmatrix} v_\alpha \\ v_\beta \end{bmatrix} = \begin{bmatrix} 1 & 0 & 0 \\ 0 & \frac{1}{\sqrt{3}} & -\frac{1}{\sqrt{3}} \end{bmatrix}, \quad \bar{v}_o = \begin{bmatrix} V_{\text{om}} \cos\theta_o \\ V_{\text{om}} \sin\theta_o \end{bmatrix}. \quad (31)$$

Some designs use v_α and v_β as inputs instead of ω_o and V_{om}. We remind the reader that the output electrical angle and the peak amplitude of the output voltage can be calculated from v_α and v_β as

$$V_{\text{om}} = \sqrt{v_\alpha^2 + v_\beta^2} \quad (32)$$

$$\theta_o = \arctan\left(\frac{v_\beta}{v_\alpha}\right). \quad (33)$$

To calculate the local averaged current supplied to the grid, we use (21), where

$$i_o = \begin{bmatrix} 1 & 0 \\ -\frac{1}{2} & \frac{\sqrt{3}}{2} \\ -\frac{1}{2} & -\frac{\sqrt{3}}{2} \end{bmatrix} \begin{bmatrix} i_\alpha \\ i_\beta \end{bmatrix}. \quad (34)$$

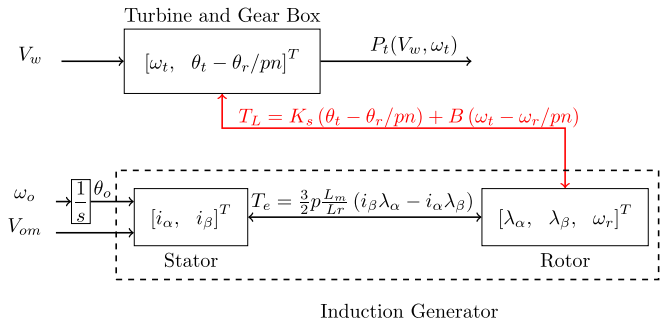

Fig. 5. Block diagram of WECS.

Denoting (5), (6), (8)–(12), (17), and (31), we summarize the state-space dynamics of WECS as follows:

$$\frac{\mathrm{d}}{\mathrm{d}t}i_\alpha=-a_0i_\alpha+a_1\lambda_\alpha+a_2\omega_r\lambda_\beta+\frac{\cos\theta_o}{\sigma L_s}V_{\mathrm{om}} \tag{35}$$

$$\frac{\mathrm{d}}{\mathrm{d}t}i_\beta=-a_0i_\beta-a_2\omega_r\lambda_\alpha+a_1\lambda_\beta+\frac{\sin\theta_o}{\sigma L_s}V_{\mathrm{om}} \tag{36}$$

$$\frac{\mathrm{d}}{\mathrm{d}t}\lambda_\alpha=a_3i_\alpha-a_4\lambda_\alpha-\omega_r\lambda_\beta \tag{37}$$

$$\frac{\mathrm{d}}{\mathrm{d}t}\lambda_\beta=a_3i_\beta-a_4\lambda_\beta+\omega_r\lambda_\alpha \tag{38}$$

$$\frac{\mathrm{d}}{\mathrm{d}t}\theta_o=\omega_o \tag{39}$$

$$\frac{\mathrm{d}}{\mathrm{d}t}\omega_r=\frac{3p^2L_m}{2L_rJ}\left(i_\beta\lambda_\alpha-i_\alpha\lambda_\beta\right)-\frac{pK_s}{\mathrm{nJ}}\tilde{\theta}-\frac{\mathrm{pB}}{\mathrm{nJ}}\left(\omega_t-\frac{\omega_r}{pn}\right) \tag{40}$$

$$\frac{\mathrm{d}}{\mathrm{d}t}\tilde{\theta}=\omega_t-\frac{\omega_r}{pn} \tag{41}$$

$$\frac{\mathrm{d}}{\mathrm{d}t}\omega_t=-\frac{P_t(V_w,\omega_t)}{J_t\omega_t}-\frac{K_s}{J_t}\tilde{\theta}-\frac{B}{J_t}\left(\omega_t-\frac{\omega_r}{pn}\right) \tag{42}$$

where ω_o and V_{om} are actuated by the MC. The wind speed V_w is an unknown disturbance that determines the MPP level of the WT. A block diagram of WECS that highlights the structure of the state-space model (35)–(42) is shown in Fig. 5. Assuming that the blade pitch angle is zero, we can employ the turbine speed, ω_t, for MPPT of the WT for wind speeds between cut-in and rated wind speed.

III. Controller Design

In many motor drive systems, it is desirable to make the drive act as a torque transducer wherein the electromagnetic torque can nearly instantaneously be made equal to a torque command. In such a system, speed or position control is dramatically simplified because the electrical dynamics of the drive become irrelevant to the speed or position control problem. In the case of induction machine drives, such performance can be achieved using a class of algorithms collectively known as FOC [18].

When flux amplitude, $\sqrt{\lambda_\alpha^2+\lambda_\beta^2}$, is regulated to a constant reference value, and considering the fact that the dynamics of ω_t are considerably slower than the electrical dynamics, we can assume that the dynamics are linear, but during flux transient, the system has nonlinear terms and it is coupled. This method can be improved by achieving exact input–output decoupling and linearization via a nonlinear state feedback that is not more complex than the conventional FOC [24].

As shown in Fig. 5, one can manipulate stator voltage amplitude, V_{om}, and its frequency, ω_o, through the MC to obtain the desired closed-loop performance for WECS. Referring to [21], [22], [24], and employing FOC idea, we introduce an integrator and an auxiliary input, u_2, to achieve input–output decoupling in WECS dynamics. Using (35)–(42) and one step of integration in front of V_{om}, the extended equations of WECS are introduced as follows:

$$\dot{x}=f(x)+g_1u_1+g_2u_2,\quad x\in\mathbb{R}^9,\quad u\in\mathbb{R}^2 \tag{43}$$

where

$$f(x)=\begin{bmatrix}-a_0x_1+a_1x_3+a_2x_4x_7+\frac{x_6\cos x_5}{\sigma L_s}\\ -a_0x_2-a_2x_3x_7+a_1x_4+\frac{x_6\sin x_5}{\sigma L_s}\\ a_3x_1-a_4x_3-x_4x_7\\ a_3x_2-a_4x_4+x_3x_7\\ 0\\ 0\\ a_5\left(x_2x_3-x_1x_4\right)-a_6x_8-a_7\left(x_9-\frac{x_7}{\mathrm{pn}}\right)\\ x_9-\frac{x_7}{\mathrm{pn}}\\ -a_9\left(x_9-\frac{x_7}{\mathrm{pn}}\right)-a_8x_8-\frac{T_t}{J_t}\end{bmatrix} \tag{44}$$

$$g_1=[0\ 0\ 0\ 0\ 1\ 0\ 0\ 0\ 0]^T \tag{45}$$

$$g_2=[0\ 0\ 0\ 0\ 0\ 1\ 0\ 0\ 0]^T \tag{46}$$

where $x=\left[i_\alpha,\ i_\beta,\ \lambda_\alpha,\ \lambda_\beta,\ \theta_o,\ V_{\mathrm{om}},\ \omega_r,\ \tilde{\theta},\ \omega_t\right]^T$, u_1 is the electrical frequency of the stator, ω_o, and u_2 is an auxiliary input (voltage amplitude rate), which generates the voltage amplitude of the stator. The constant parameters are defined in the Table II (see Appendix).

From (4) and Fig. 4, we know that the turbine speed controls the power generation. In addition, we are interested in decoupling the rotor flux and electromagnetic torque to obtain the benefits of FOC. For these reasons, we introduce turbine speed, $y_1=\omega_t$, and flux amplitude, $\eta_1=|\lambda|^2$, as measurable outputs. For future analysis, we assume that the power coefficient and wind speed function satisfy following assumption.

Assumption 1: The power coefficient $C_p(\omega_t, V_w)$ and wind speed function $V_w(t)$ are bounded C^3 functions with bounded derivatives. Hence, the mechanical torque, T_t, is a bounded C^3 function with bounded derivatives.

Based on the selected outputs and having Assumption 1 satisfied, we apply feedback linearization with the following change of variables to WECS dynamics:

$$y_1=\Psi_1(x)=x_9 \tag{47}$$

$$y_2=\mathcal{L}_f\Psi_1(x)=-a_9\left(x_9-\frac{x_7}{pn}\right)-a_8x_8-\frac{T_t}{J_t} \tag{48}$$

$$y_3=\mathcal{L}_f^2\Psi_1(x)=b_0\xi_q+b_1\mathcal{L}_f\Psi_1(x)+b_2x_8+b_3\frac{T_t}{J_t}-\frac{\dot{T}_t}{J_t} \tag{49}$$

$$\begin{aligned}y_4&=\mathcal{L}_f^3\Psi_1(x)\\&=b_4\mathcal{L}_f^2\Psi_1(x)+b_5\mathcal{L}_f\Psi_1(x)+b_6x_8\\&\quad-\frac{b_0}{\sigma L_s}x_6\lambda_q-x_7\left(b_7\Psi_2(x)+b_8\mathcal{L}_f\Psi_2(x)\right)\\&\quad+b_9\frac{T_t}{J_t}+b_{10}\frac{\dot{T}_t}{J_t}-\frac{\ddot{T}_t}{J_t}\end{aligned} \tag{50}$$

$$\eta_1 = \Psi_2(x) = x_3^2 + x_4^2 \tag{51}$$

$$\eta_2 = \mathcal{L}_f \Psi_2(x) = 2a_3\xi_d - 2a_4\Psi_2(x) \tag{52}$$

$$\begin{aligned}\eta_3 &= \mathcal{L}_f^2 \Psi_2(x) \\ &= b_{12}\Psi_2(x) - b_{11}\mathcal{L}_f\Psi_2(x) \\ &\quad + b_{13}x_7\left(\mathcal{L}_f^2\Psi_1(x) - b_1\mathcal{L}_f\Psi_1(x) - b_2x_8 - b_3\frac{T_t}{J_t} + \frac{\dot{T}_t}{J_t}\right) \\ &\quad + 2a_3^2 i_s + \frac{2a_3}{\sigma L_s}x_6\lambda_d\end{aligned} \tag{53}$$

$$\Delta = x_8 \tag{54}$$

$$\varphi = \arctan\left(\frac{x_4}{x_3}\right) \tag{55}$$

where $\xi_d = x_1x_3 + x_2x_4$, $\xi_q = x_2x_3 - x_1x_4$, $i_s = i_\alpha^2 + i_\beta^2$ and

$$\begin{bmatrix} \lambda_d \\ \lambda_q \end{bmatrix} = \begin{bmatrix} \cos x_5 & \sin x_5 \\ -\sin x_5 & \cos x_5 \end{bmatrix}\begin{bmatrix} x_3 \\ x_4 \end{bmatrix}. \tag{56}$$

The inverse transformation of (47)–(55) is

$$\begin{bmatrix} x_1 \\ x_2 \end{bmatrix} = \frac{1}{\sqrt{\eta_1}}\begin{bmatrix} \cos\varphi & -\sin\varphi \\ \sin\varphi & \cos\varphi \end{bmatrix}\begin{bmatrix} \Psi_d \\ \Psi_q \end{bmatrix} \tag{57}$$

$$x_3 = \sqrt{\eta_1}\cos\varphi \tag{58}$$

$$x_4 = \sqrt{\eta_1}\sin\varphi \tag{59}$$

$$x_5 = \arctan\left(\frac{\Upsilon_\beta}{\Upsilon_\alpha}\right) \tag{60}$$

$$x_6 = \sqrt{\Upsilon_\alpha^2 + \Upsilon_\beta^2} \tag{61}$$

$$x_7 = pn\left(y_1 + \frac{y_2}{a_9} + \frac{a_8}{a_9}\Delta + \frac{T_t}{a_9J_t}\right) \tag{62}$$

$$x_8 = \Delta \tag{63}$$

$$x_9 = y_1 \tag{64}$$

where

$$\Psi_d = \frac{\eta_2 + 2a_4\eta_1}{2a_3} \tag{65}$$

$$\Psi_q = \frac{1}{b_0}\left(y_3 - b_1y_2 - b_2\Delta - b_3\frac{T_t}{J_t} + \frac{\dot{T}_t}{J_t}\right) \tag{66}$$

$$\begin{bmatrix} \Upsilon_\alpha \\ \Upsilon_\beta \end{bmatrix} = \frac{1}{\sqrt{\eta_1}}\begin{bmatrix} \cos\varphi & -\sin\varphi \\ \sin\varphi & \cos\varphi \end{bmatrix}\begin{bmatrix} \Phi_d \\ \Phi_q \end{bmatrix} \tag{67}$$

with

$$\Phi_d = \frac{\sigma L_s}{2a_3}(\eta_3 + 2a_4\eta_2 - 2a_1a_3\eta_1 - 2a_3^2 i_s + 2a_3(a_0 + a_4)\Psi_d) \tag{68}$$

$$\begin{aligned}\Phi_q = \frac{\sigma L_s}{b_0}\Bigg(&y_4 - b_1y_3 + \frac{a_8^2}{a_9^2}y_2 + \frac{a_8^3}{a_9^2}\Delta + b_0(a_0 + a_4)\Psi_q \\ &+ b_0x_7(\Psi_d + a_2\eta_1) + \frac{a_8^2}{a_9^2}\frac{T_t}{J_t} - b_3\frac{\dot{T}_t}{J_t} + \frac{\ddot{T}_t}{J_t}\Bigg).\end{aligned} \tag{69}$$

The change of variables results in the following equations:

$$\dot{y}_1 = y_2 \tag{70}$$

$$\dot{y}_2 = y_3 \tag{71}$$

$$\dot{y}_3 = y_4 \tag{72}$$

$$\dot{y}_4 = G_1 + \frac{b_0\lambda_d}{\sigma L_s}x_6u_1 - \frac{b_0\lambda_q}{\sigma L_s}u_2 \tag{73}$$

$$\dot{\eta}_1 = \eta_2 \tag{74}$$

$$\dot{\eta}_2 = \eta_3 \tag{75}$$

$$\dot{\eta}_3 = G_2 + \frac{2a_3\lambda_q}{\sigma L_s}x_6u_1 + \frac{2a_3\lambda_d}{\sigma L_s}u_2 \tag{76}$$

$$\dot{\Delta} = -\frac{y_2}{a_9} - \frac{a_8}{a_9}\Delta - \frac{T_t}{a_9J_t} \tag{77}$$

$$\dot{\varphi} = \omega_r + \frac{a_3}{b_0\eta_1}\left(y_3 - b_1y_2 - b_2\Delta - b_3\frac{T_t}{J_t} + \frac{\dot{T}_t}{J_t}\right) \tag{78}$$

where (77) and (78) are zero dynamics of the system and

$$\begin{aligned}G_1 = &b_4y_4 + b_5y_3 - \frac{b_6}{a_9}y_2 - \frac{a_8b_6}{a_9}\Delta \\ &- \frac{b_0x_6}{\sigma L_s}\left(a_3i_d - a_4\lambda_q + x_7\lambda_d\right) \\ &- f_7(x)\left(b_7\eta_1 + b_8\eta_2\right) - x_7\left(b_7\eta_2 + b_8\eta_3\right) \\ &- \frac{b_6}{a_9}\frac{T_t}{J_t} + b_9\frac{\dot{T}_t}{J_t} + b_{10}\frac{\ddot{T}_t}{J_t} - \frac{\dddot{T}_t}{J_t}\end{aligned} \tag{79}$$

$$\begin{aligned}G_2 = &-b_{11}\eta_3 + b_{12}\eta_2 + b_{13}f_7(x)\xi_q \\ &+ b_{13}x_7\left(y_4 - b_1y_3 - b_2f_8(x) - b_3\frac{\dot{T}_t}{J_t} + \frac{\ddot{T}_t}{J_t}\right) \\ &+ 4a_3^2\left(a_1\xi_d - a_0i_s - a_2x_7\xi_q + \frac{2x_6}{\sigma L_s}i_d\right) \\ &+ \frac{2a_3x_6}{\sigma L_s}\left(a_3i_d - a_4\lambda_d - x_7\lambda_q\right)\end{aligned} \tag{80}$$

where

$$\begin{bmatrix} i_d \\ i_q \end{bmatrix} = \begin{bmatrix} \cos x_5 & \sin x_5 \\ -\sin x_5 & \cos x_5 \end{bmatrix}\begin{bmatrix} x_1 \\ x_2 \end{bmatrix}. \tag{81}$$

Defining control signals as follows:

$$\begin{bmatrix} x_6u_1 \\ u_2 \end{bmatrix} = \frac{\sigma L_s}{\sqrt{\eta_1}}\begin{bmatrix} \cos(\varphi - \theta_o) & \sin(\varphi - \theta_o) \\ -\sin(\varphi - \theta_o) & \cos(\varphi - \theta_o) \end{bmatrix}\begin{bmatrix} \frac{v_1 - G_1}{b_0} \\ \frac{v_2 - G_2}{2a_3} \end{bmatrix} \tag{82}$$

and applying another step of change of variables

$$z = \left[y_1 - \omega_t^{\text{ref}},\ y_2,\ y_3,\ y_4\right]^T \tag{83}$$

$$\zeta = \left[\eta_1 - \left(|\lambda|^{\text{ref}}\right)^2,\ \eta_2,\ \eta_3\right]^T \tag{84}$$

we obtain

$$\dot{z}_1 = z_2 \tag{85}$$

$$\dot{z}_2 = z_3 \tag{86}$$

$$\dot{z}_3 = z_4 \tag{87}$$

$$\dot{z}_4 = v_1 \tag{88}$$

$$\dot{\zeta}_1 = \zeta_2 \tag{89}$$

$$\dot{\zeta}_2 = \zeta_3 \tag{90}$$

$$\dot{\zeta}_3 = v_2 \tag{91}$$

$$\dot{\Delta} = -\frac{z_2}{a_9} - \frac{a_8}{a_9}\Delta - \frac{T_t}{a_9J_t} \tag{92}$$

$$\dot{\varphi} = \omega_r + \frac{a_3}{b_0\eta_1}\left(z_3 - b_1z_2 - b_2\Delta - b_3\frac{T_t}{J_t} + \frac{\dot{T}_t}{J_t}\right). \tag{93}$$

Linear state feedback

$$v_1 = -k_1'z_1 - k_2'z_2 - k_3'z_3 - k_4'z_4 \tag{94}$$

$$v_2 = -k_1''\zeta_1 - k_2''\zeta_2 - k_3''\zeta_3 \tag{95}$$

stabilizes this system, which results in the regulation of turbine speed, $\omega_t = y_1$, to its reference value ω_t^{ref} while amplitude of rotor flux, $|\lambda| = \sqrt{\eta_1}$, has converged to its desired value $|\lambda|^{\text{ref}}$. Moreover, the convergence rate of

$$\Sigma = \left[i_\alpha^2 + i_\beta^2,\ \lambda_\alpha^2 + \lambda_\beta^2,\ \omega_r,\ \omega_o,\ \omega_t,\ \tilde{\theta}\right]^T \tag{96}$$

is exponential, and, in fact, it is independent of the selection of the reference frame.

Remark 2: The closed-loop system (85)–(93) is input–output decoupled and linear. The input–output map consists of fourth-order and third-order systems. This allows for an independent regulation (or tracking) of the outputs using control signals (94) and (95). Transient responses are now decoupled also when $|\lambda|^{\text{ref}}$ is varied, even independently of ω_t^{ref}. This is an improvement over FOC.

Remark 3: As in FOC, while measurements of $(i_\alpha, i_\beta, \omega_r)$ are available, measurements of $(\lambda_\alpha, \lambda_\beta)$ require installing flux sensing coils or Hall effect transducers in the stator, which is not realistic in general purpose squirrel cage machines. However, $(\lambda_\alpha, \lambda_\beta)$ flux components can be reconstructed by means of an asymptotic observer of reduced order, as shown in [7].

Furthermore, the a-phase voltage equation can be expressed as

$$v_{\text{as}} = R_{si_{as}} + \frac{\mathrm{d}}{\mathrm{d}t}\lambda_{as}. \tag{97}$$

For steady-state conditions at intermediate to high speeds wherein the flux linkage term dominates the resistive term in the voltage equation, the magnitude of the applied voltage is related to the magnitude of the stator flux linkage by

$$V_s = \omega_o \Lambda_s \tag{98}$$

which suggests that to maintain constant flux linkage (to avoid saturation), the stator voltage magnitude should be proportional to frequency [18]. Since we regulate the flux to a constant value, the voltage will be proportional to the electrical frequency. In the next section, we use our designed controller combined with an ES algorithm to extract maximum power from WECS under various wind speeds.

IV. MPPT Using ES

There are three main MPPT techniques for WECS: wind speed measurement (WSM), P&O, and PSF. Measurement of wind velocity is required in WSM method. It is clear that accurate measurement of wind velocity is complicated and increases the system cost. Since the P&O method adds delay, it is not practical for medium- and large-inertia WT systems. To implement PSF control, maximum power curve (maximum power versus turbine speed) is required. The maximum power is then tracked by turbine speed control [5].

Fig. 6 shows a typical block diagram of P&O using direct FOC for the IG [9], [36]. To implement FOC scheme, the rotor flux magnitude $|\lambda|$ and its angle φ are identified by the rotor flux calculator based on the measured stator voltage (v_o) and current (i_o). The turbine speed reference ω_e^{ref} is generated by the MPPT scheme.

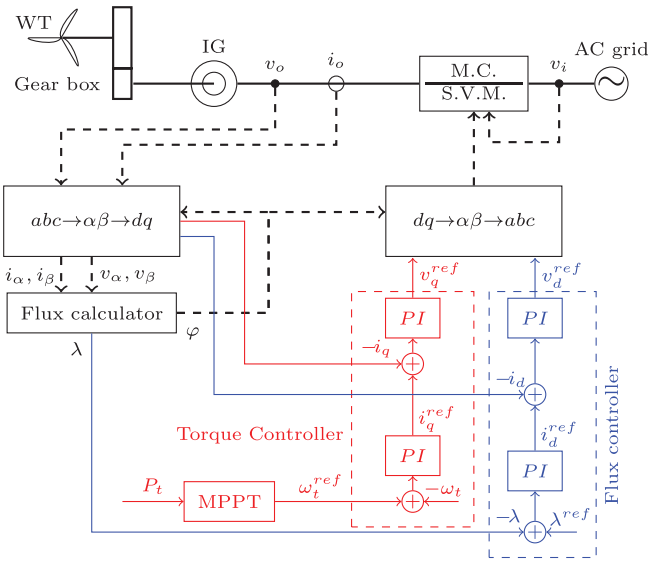

Fig. 6. MPPT for a WECS based on P&O using conventional direct FOC. The abc$\to\alpha\beta$ and its inverse follows from (31) and (34). The $\alpha\beta\to$dq and its inverse follows from (81). The flux calculator uses (51) and (55). The controllers are proportional-integral.

To overcome challenges attached with the conventional power control and optimization algorithms and to remove the dependence of the MPPT algorithm on the system modeling and identification, we propose ES algorithm, which is a nonmodel-based real-time optimization technique to MPPT of WECS. First, we present ES without the inner-loop control to clarify the advantages of the proposed controller on the closed-loop performance of the system.

The proposed models for power coefficient and turbine power in (3) and (4) are for simulation purposes. In this paper, we assume that we have access to turbine power measurements and we can manipulate the turbine speed through the MC. Furthermore, we do not have a model of the power coefficient or turbine power. However, we know that the turbine power map has one MPP under any wind speed, which helps us to present the following assumption.

Assumption 2: The following holds for the turbine power map around its MPP for $V_{\text{cut}-\text{in}} < V_w < V_{\text{rated}}$ (see Fig. 4)

$$\frac{\partial P_t(V_w, \omega_t)}{\partial \omega_t}(\omega_t^*) = 0 \tag{99}$$

$$\frac{\partial^2 P_t(V_w, \omega_t)}{\partial \omega_t^2}(\omega_t^*) < 0 \tag{100}$$

where ω_t^* is the optimal turbine speed.

Following statement explains actual relation between turbine speed and stator electrical frequency.

Remark 4: The torque–speed characteristic of an induction machine is normally quite steep in the neighborhood of stator electrical frequency (synchronous speed), ω_o, and so the electrical rotor speed, ω_r, will be near the synchronous speed. This means that changing the reference value of the turbine speed, ω_t, which translates in variation of the electrical rotor speed eventually results in changing the stator electrical frequency [18]. Thus, by controlling the stator electrical frequency, one can approximately control the turbine speed or vice versa.

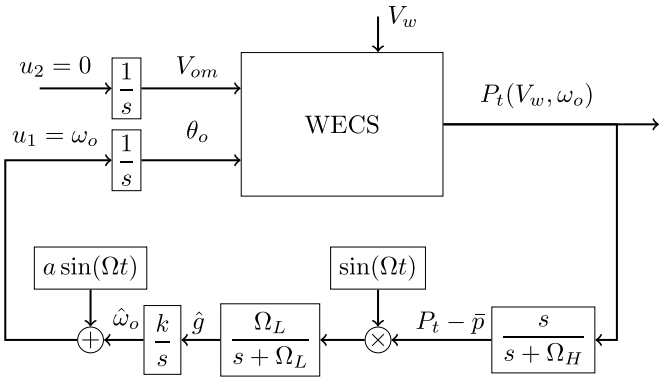

Fig. 7. MPPT for a WECS based on ES without the inner-loop control.

A schematic diagram of MPPT for WECS with ES without inner-loop nonlinear control is shown in Fig. 7. Remark 4 implies that the power is parameterized by ω_o, which is estimated by ES loop. The other input for WECS that generates the voltage amplitude has been set to zero, which means the stator voltage has a constant peak amplitude. The parameters of the ES loop are defined as follows:

$$\Omega = \epsilon\Omega' \tag{101}$$

$$\Omega_H = \epsilon\Omega'_H = \epsilon\delta\Omega''_H = O(\epsilon\delta) \tag{102}$$

$$\Omega_L = \epsilon\Omega'_L = \epsilon\delta\Omega''_L = O(\epsilon\delta) \tag{103}$$

$$k = \epsilon k' = \epsilon\delta k'' = O(\epsilon\delta) \tag{104}$$

where Ω' is a rational number, ϵ and δ are small positive constants, and Ω''_H, Ω''_L, and k'' are $O(1)$ positive constants. In addition, a needs to be small.

Stability analysis of the ES without the inner-loop control follows the same steps as [19]. To start with the proof, we assume that the turbine shaft is rigid. Hence, the WECS dynamics is simplified as follows:

$$\dot{X} = F(X, U, V_{\rm om}, V_w) \tag{105}$$

$$P_t(V_w, X_5) = 55.115\rho A \frac{\frac{{\rm pn}V_w}{RX_5} - 0.09}{\exp\left(\frac{{\rm pn}V_w}{RX_5} - 0.003\right)} V_w^3 \tag{106}$$

where $X = \left[i_d,\ i_q,\ \lambda_d,\ \lambda_q,\ \omega_r\right]^T$, $U = \omega_o$, and

$$F = \begin{bmatrix} -a_0X_1 + UX_2 + a_1X_3 + a_2X_5X_4 + \frac{V_{\rm om}}{\sigma L_s} \\ -UX_1 - a_0X_2 - a_2X_5X_3 + a_1X_4 \\ a_3X_1 - a_4X_3 + (U - X_5)X_4 \\ a_3X_2 - (U - X_5)X_3 - a_4X_4 \\ a_5(X_2X_3 - X_1X_4) + \frac{p}{{\rm n}J}T_t(X_5, V_w) \end{bmatrix}. \tag{107}$$

Note that, in this case, $\omega_t = \omega_r/({\rm pn})$. The IG dynamics are presented in synchronous frame, namely the frame, which rotates in speed of the stator electrical frequency, U. The equilibrium, $F(X, U, V_{\rm om}, V_w) = 0$, is parameterized by U, $V_{\rm om}$, and V_w. We assume that the stator voltage amplitude, $V_{\rm om}$, and the wind speed are fixed at a constant level, which make the equilibrium parameterized only by U, i.e., $X_e = l(U)$. Moreover, the Jacobian of IG has left-half plane poles at each equilibrium point on the negative slope of the torque–speed characteristic, as shown in [18, Sec. 8.5], which makes the system exponentially stable. Our analytical results for this case (no inner-loop control) are summarized in the theorem below.

Theorem 1: Consider (105) with constant V_w and $V_{\rm om}$ under Assumption 2 and recall that for any fixed electrical frequency, $U = \omega_o$, (105) is exponentially stable at the negative slope of the IG torque–speed characteristic, as shown in [18, Sec. 8.5]. For the system in Fig. 7, there exists a ball of initial conditions around the point $(X, \hat{\omega}_o, \hat{g}, \bar{p}) = (l(\omega_o^*), \omega_o^*, 0, P_t^*)$ and constants $\bar{\epsilon}$, $\bar{\delta}$, and $\bar{a}$ such that for all $\epsilon \in (0, \bar{\epsilon})$, $\delta \in (0, \bar{\delta})$, and $a \in (0, \bar{a})$, the solution $[X(t), \hat{\omega}_o(t), \hat{g}(t), \bar{p}(t)]$ exponentially converges to an $O(\epsilon + \delta + a)$-neighborhood of that point. Furthermore, $P_t(t)$ converges to an $O(\epsilon + \delta + a)$-neighborhood of P_t^*.

The turbine power measurement is fed into ES scheme. The optimization parameter for ES without the inner-loop control, Fig. 7, is the electrical frequency of IG stator, ω_o. Stability of system dynamics is required for convergence of ES algorithm to its peak point. It is also required that the ES algorithm works more slowly than the WECS system dynamics. As previously mentioned, since WECS in Fig. 7 without the inner-loop controller shows a slow transient, the entire system has a lengthy convergence process, which results in low power efficiency.

We propose to employ the nonlinear control from Section III to achieve the desired closed-loop performance, including faster response time (high power efficiency), and preventing magnetic saturation. Our proposed ES scheme with the inner-loop control is shown in Fig. 8. In this case, the reference inputs of the inner-loop control are $\omega_t^{\rm ref}$ and $|\lambda|^{\rm ref}$. From Assumption 2, we know that the MPP is parameterized by the optimal turbine speed at each wind speed, which is estimated by the ES loop. The other control input $|\lambda|^{\rm ref}$ defines the level of the flux linkage of the rotor, which prevents IG from magnetic saturation.

Remark 5: From (2) and (4), we observe that the torque on the WT shaft depends on the wind speed and turbine speed. In addition, to implement the controller in Section III, we need to have access to the first-, second-, and third-order derivatives of the torque.

1) By Assumption 1 and because of fast response dynamics of the inner loop and the WT, it is reasonable to assume that (for the inner-loop design shown in Fig. 8) variation of the wind speed is negligible in comparison with the dynamics of controller system.
2) Since the convergence time of the estimate of the turbine speed generated by ES loop is considerably slower than the response time of the controller system, we can assume that turbine speed reference is constant in comparison with the fast dynamics of the controller system.

Using this observation and from (2) and (4), we can assume that the variation of mechanical torque, computed as P_t/ω_t, and its derivatives are negligible in comparison with the dynamics of the controller system. In addition, the inner loop becomes independent of the turbine power map, but it still relies on the IG dynamics and measurements of the turbine power, the turbine speed, ω_t, and angle displacement caused by the shaft model, $\tilde{\theta}$. The ES algorithm generates the estimate of the turbine speed, which is the reference input for the inner loop and maximizes the power generated by the WT, and

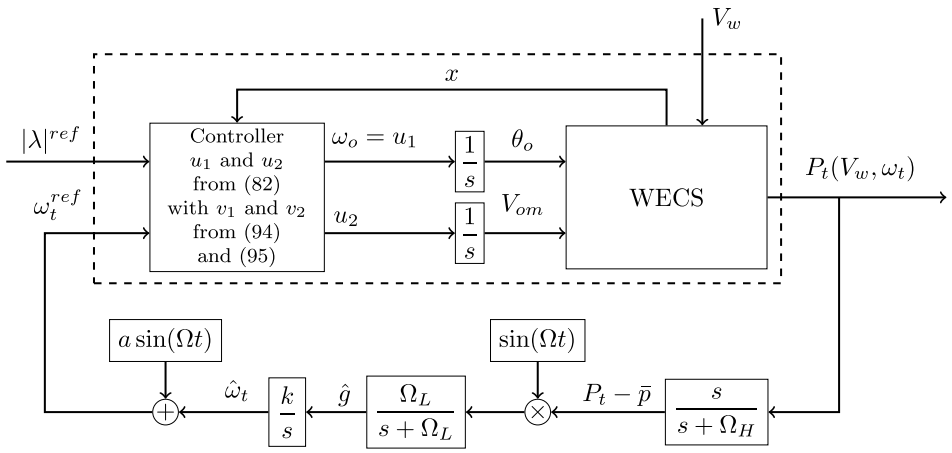

Fig. 8. ES for MPPT in WECS with the inner-loop control.

governs the system to its MPP, despite high uncertainty in the turbine power map.

Combination of the controller and WECS includes fast dynamics and ES algorithm contains slow- and medium-speed dynamics. The ES algorithm estimates the optimal turbine speed, $\omega_t^{\text{ref}} = \omega_t^*$, which can be considered as a constant value with respect to the fast dynamics of the controller system. The ES scheme estimates the gradient of the cost function, P_t, by injecting a small perturbation, $a\sin(\Omega t)$, which is very slow with respect to the dynamics of the controller system and its amplitude is enough small in comparison with ω_t. The high-pass filter removes the dc part of the signal. The multiplication of the resulting signal by $\sin(\Omega t)$ creates an estimate of the gradient of the cost function, which is smoothed using a low-pass filter. When ω_t is larger than its optimal value, the estimate of the gradient, $\hat{g}$, is negative and causes ω_t to decrease. On the other hand, when ω_t is smaller than ω_t^*, then $\hat{g} > 0$, which increases the ω_t toward ω_t^*. It should be noted that Ω is small enough in comparison with the slowest dynamic of the controller system, with an order less than 10%.

The analytical results for the closed-loop system with the ES design are summarized in the theorem below, the proof of which also follows from [19]. We remind the reader that in the singular perturbation analysis of [19] the dynamics of $\dot{\varphi}$ can be neglected without hurting the proof.

Theorem 2: Consider the feedback system in Fig. 8, which includes the plant (43) under Assumption 1 and 2 with control input (82), where v_1 and v_2 are defined as (94) and (95). Recall that Remark 5 is in place. There exists a ball of initial conditions around the point $(\Sigma, \hat{\omega}_t, \hat{g}, \bar{p}) = (\ell(\omega_t^*), \omega_t^*, 0, P_t^*)$, and constants $\bar{\epsilon}$, $\bar{\delta}$, and $\bar{a}$ such that for all $\epsilon \in (0, \bar{\epsilon})$, $\delta \in (0, \bar{\delta})$, and $a \in (0, \bar{a})$, the solution $(\Sigma(t), \hat{\omega}_t(t), \hat{g}(t), \bar{p}(t))$ exponentially converges to an $O(\epsilon+\delta+a)$-neighborhood of that point. Furthermore, $P_t(t)$ converges to an $O(\epsilon+\delta+a)$-neighborhood of P_t^*. In addition, the magnetic saturation is avoided by selecting a constant reference for the flux amplitude, $|\lambda|^{\text{ref}}$.

V. Simulation Result

As we mentioned earlier, response time of the ES design without the inner loop is considerably slow, which results in a very low power efficiency. However, we present one simulation that compares the response of the design without the inner loop, as shown in Fig. 7, to our proposed algorithm, as shown in Fig. 8, which shows the role of the inner loop. In addition, We compare the performance of our proposed algorithm to the conventional algorithm shown in Fig. 6. By appropriate selection of the feedback gains in (94) and (95) and using (82), we can obtain the desired closed-loop response time. Control signals are designed such that the poles of z-error subsystem (85)–(88) and ζ-error subsystems (89)–(91) move to $P_z = [-550 \ -600 \ -650 \ -700]$ and $P_\zeta = [-570 \ -620 \ -670]$, respectively. The response time of the closed-loop system is about 20 ms, which is 25 times faster than the open-loop system. We select the parameters of the ES loop as follows: $\Omega = 100$ rad/s, $\Omega_L = 6$ rad/s, $\Omega_H = 5$ rad/s, $a = 0.1$, and $k = 0.004$. The amplitude of the perturbation function is selected proportional to the turbine speed. Higher values of a reduce the precision of the MPPT, as shown in Theorem 2.

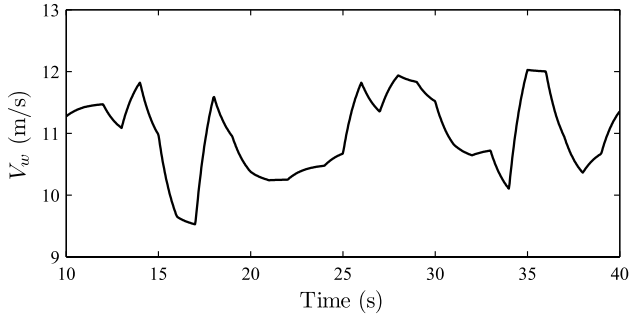

Fig. 9. Variation of wind speed versus time.

We show a time frame of 30 s to visualize the differences between our proposed algorithm and the two other algorithms, properly. Fig. 9 shows the wind regime applied to the WECS. The MPPT process is shown in Fig. 10. It is clear from Fig. 11 that our proposed algorithm stays very close to C_p^* despite fast changes in wind speed. The extracted energy by our proposed algorithm is 2.36% higher than the extracted energy by the conventional MPPT and FOC. As we expected, the power efficiency of the ES design without the inner loop is low and, as shown in Fig. 11, the power coefficient almost always stays far from C_p^*. We have verified the robustness of our proposed

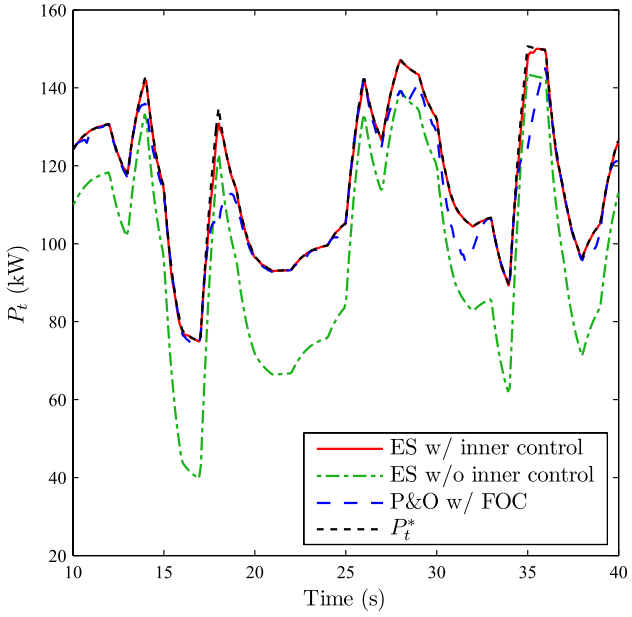

Fig. 10. MPPT, (solid red line) our proposed algorithm, (dashed-dotted green line) ES without inner loop, (dashed blue line) conventional P&O with FOC, and (dotted black line) maximum power available to the WECS.

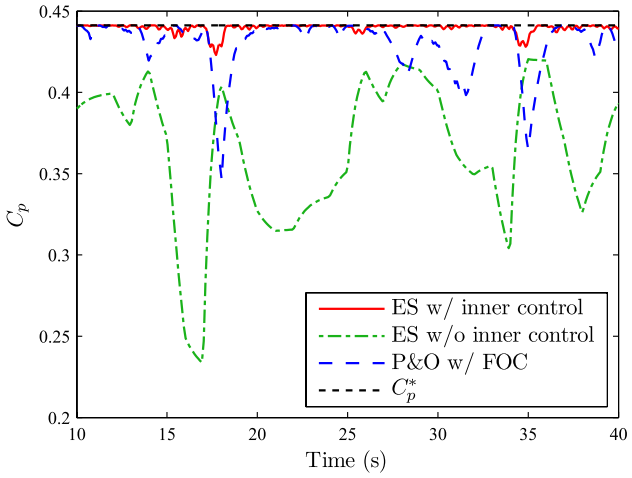

Fig. 11. Variation of power coefficient, (solid red line) our proposed algorithm, (dashed-dotted green line) ES without inner loop, (dashed blue line) conventional P&O with FOC, and (dotted black line) maximum power coefficient.

algorithm by adding different amount of perturbation to the rotor and stator resistance and inductance. We present one of our robustness simulations with a 100% increment in rotor resistance at time 15 s and then back to its nominal value at time 25 s. While as shown in Fig. 12, the performance of the proposed algorithms remains unchanged, the conventional MPPT algorithm is not able to attenuate the effect of the disturbance, as shown in Fig. 13.

The proposed algorithm combines two well-known control algorithms, namely feedback linearization based on the FOC concept and ES, to achieve MPPT in a WECS operating in Region II. Our algorithm provides perfect input–output decoupling and guarantees a larger domain of attraction, which increases performance robustness with respect to the system parameters. However, one may question the implementation

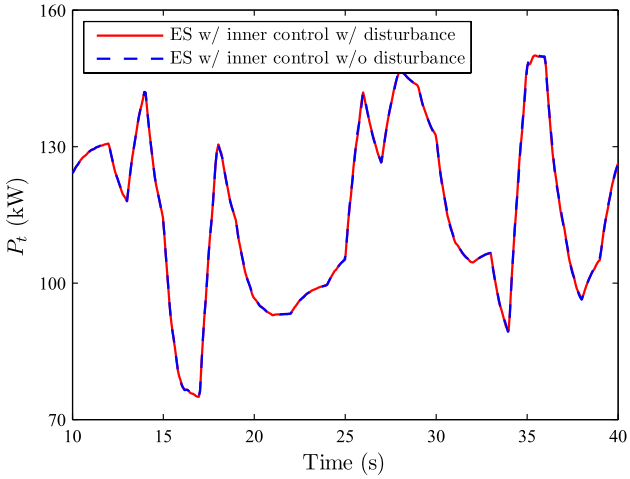

Fig. 12. Robustness analysis with a 100% increment in the rotor resistor at time 15 s and back to its nominal value at time 25 s for the proposed algorithm. Variation of turbine power (solid red line) with perturbation and (dashed blue line) without perturbation.

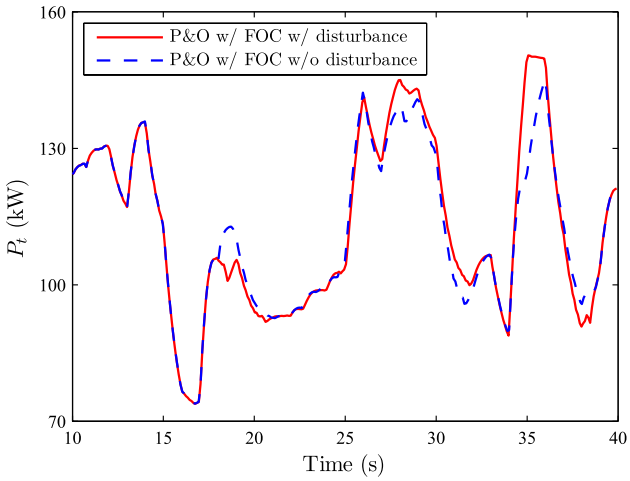

Fig. 13. Robustness analysis with a 100% increment in the rotor resistor at time 15 s and back to its nominal value at time 25 s for conventional P&O with FOC. Variation of turbine power (solid red line) with perturbation and (dashed blue line) without perturbation.

complexity of the proposed algorithm. Clearly higher power efficiency is our aim and to this end, we have to sacrifice the simplicity in favor of harvesting more energy. Since the WECS runs for a long period of time, a small improvement in power efficiency guarantees extracting a higher energy level and leads to cost reduction of the WECS.

VI. Conclusion

We presented an ES algorithm to extract maximum power from a WECS for wind speed from cut-in wind speed to rated wind speed. The design employed an inner-loop nonlinear controller based on field-oriented approach and feedback linearization technique to control the closed-loop transient performance, with respect to which the ES had to be tuned. Without this inner-loop control, the convergence rate of the closed-loop system would be much slower. This optimization/control algorithm can readily be extended to other classes of WECS without major changes. The main parameters that need to be adjusted are the probing frequency and amplitude of the perturbation signal. Furthermore, the proposed control strategy prevents magnetic saturation in the IG.

APPENDIX

TABLE I

DEFINITIONS OF PARAMETERS AND THEIR NUMERICAL VALUES

Parameter	Definition	Value	Unit
R	Blade length	10	m
β	Blade pitch angle	0	rad
A	Blade impact area	πR^2	m^2
V_w	Wind speed	–	m/s
ρ	Air density	1.25	kg/m^3
J_t	Turbine inertia	100	Kgm^2
ω_t	Turbine speed	–	rad/s
θ_t	Turbine angel	–	rad
n	Gear box ratio	20	–
K_s	Stiffness coefficient	2×10^6	Nm/rad
B	Damping coefficient	5×10^5	Nm/rad/s
p	Number of pole pairs of SCIG	2	–
L_{ls}	Stator leakage inductance	3.2	mH
L_{lr}	Rotor leakage inductance	3.2	mH
L_m	Magnetizing inductance	143.36	mH
J	Moment of inertia of SCIG	11.06	Kgm^2
R_s	Stator resistance	0.262	Ω
R_r	Rotor resistance	0.187	Ω
ω_r	Rotor electrical frequency	–	rad/s
ω_o	Stator electrical frequency	–	rad/s
V_{im}	Input voltage peak amplitude	1880	V

TABLE II

CONSTANT PARAMETERS

a_0	$a_2a_3 + R_s/(\sigma L_s)$	b_0	$a_5a_9/(pn)$
a_1	a_2a_4	b_1	$a_8/a_9 + a_7/(pn) - a_9$
a_2	$L_m/(\sigma L_s L_r)$	b_2	a_8^2/a_9
a_3	$L_m R_r/L_r$	b_3	$a_8/a_9 + a_7/(pn)$
a_4	R_r/L_r	b_4	$b_1 - a_0 - a_4$
a_5	$3p^2 L_m/(2JL_r)$	b_5	$a_0b_1 + a_4b_1 - b_2/a_9$
a_6	$pK_s/(Jn)$	b_6	$a_0b_2 + a_4b_2 - a_8b_2/a_9$
a_7	$pB/(Jn)$	b_7	$a_2b_0 + a_4b_0/a_3$
a_8	K_s/J_t	b_8	$b_0/(2a_3)$
a_9	B/J_t	b_9	$a_0b_3 + a_4b_3 - b_2/a_9$
b_{12}	$2a_1a_3 - 2a_0a_4 - 2a_4^2$	b_{10}	$b_3 - a_0 - a_4$
b_{13}	$2a_3/b_0$	b_{11}	$a_0 + 3a_4$

REFERENCES

[1] P. M. Anderson and A. Bose, "Stability simulation of wind turbine systems," *IEEE Trans. Power App. Syst.*, vol. 102, no. 12, pp. 3791–3795, Dec. 1983.

[2] K. B. Ariyur and M. Krstić, *Real-Time Optimization by Extremum Seeking Feedback*. New York, NY, USA: Wiley, 2003.

[3] A. Banaszuk, K. B. Ariyur, M. Krstić, and C. A. Jacobson, "An adaptive algorithm for control of combustion instability," *Automatica*, vol. 40, no. 11, pp. 1965–1972, 2004.

[4] S. M. Barakati, "Modeling and controller design of a wind energy conversion system including a matrix converter," Ph.D. dissertation, Dept. Electr. Comput. Eng., University of Waterloo, Waterloo, ON, Canada, 2008.

[5] S. M. Barakati, M. Kazerani, and J. D. Aplevich, "Maximum power tracking control for a wind turbine system including a matrix converter," *IEEE Trans. Energy Convers.*, vol. 24, no. 3, pp. 705–713, Sep. 2009.

[6] R. Becker, R. King, R. Petz, and W. Nitsche, "Adaptive closed-loop separation control on a high-lift configuration using extremum seeking," *AIAA J.*, vol. 45, no. 6, pp. 1382–1392, 2007.

[7] A. Bellini, G. Figalli, and G. Ulivi, "Analysis and design of a microcomputer-based observer for an induction machine," *Automatica*, vol. 24, no. 4, pp. 549–555, 1988.

[8] A. I. Bratcu, E. C. Iulian Munteanu, and S. Epure, "Energetic optimization of variable speed wind energy conversion systems by extremum seeking control," in *Proc. Int. Conf. Comput. Tool*, 2007, pp. 2536–2541.

[9] R. Cardenas, R. Pena, J. Clare, and P. Wheeler, "Analytical and experimental evaluation of a WECS based on a cage induction generator fed by a matrix converter," *IEEE Trans. Energy Convers.*, vol. 26, no. 1, pp. 204–215, Mar. 2011.

[10] D. Carnevale, A. Astolfi, C. Centioli, S. Podda, V. Vitale, and L. Zaccarian, "A new extremum seeking technique and its application to maximize RF heating on FTU," *Fusion Eng. Des.*, vol. 84, pp. 554–558, Jun. 2009.

[11] M. Guay, M. Perrier, and D. Dochain, "Adaptive extremum seeking control of nonisothermal continuous stirred reactors," *Chem. Eng. Sci.*, vol. 60, no. 13, pp. 3671–3681, 2005.

[12] L. Huber and D. Borojevic, "Space vector modulated three-phase to three-phase matrix converter with input power factor correction," *IEEE Trans. Ind. Appl.*, vol. 31, no. 6, pp. 1234–1246, Nov./Dec. 1995.

[13] K. E. Johnson, L. Y. Pao, M. J. Balas, and L. J. Fingersh, "Control of variable-speed wind turbines: Standard and adaptive techniques for maximizing energy capture," *IEEE Control Syst. Mag.*, vol. 26, no. 3, pp. 70–81, Jun. 2006.

[14] S. J. Johnson and C. P. C. van Dam, "Active load control techniques for wind turbines," Sandia Nat. Lab., Albuquerque, NM, USA, Tech. Rep. SAND2008-4809, 2008.

[15] S. M. R. Kazmi, H. Goto, H.-J. Guo, and O. Ichinokura, "A novel algorithm for fast and efficient speed-sensorless maximum power point tracking in wind energy conversion systems," *IEEE Trans. Ind. Electron.*, vol. 58, no. 1, pp. 29–36, Jan. 2011.

[16] N. Killingsworth and M. Krstić, "Auto-tuning of PID controllers via extremum seeking," in *Proc. Amer. Control Conf.*, vol. 4. Jun. 2005, pp. 2251–2256.

[17] M. Komatsu, H. Miyamoto, H. Ohmori, and A. Sano, "Output maximization control of wind turbine based on extremum control strategy," in *Proc. Amer. Control Conf.*, 2001, pp. 1739–1740.

[18] P. C. Krause, O. Wasynczuk, and S. D. Sudhoff, *Analysis of Electric Machinery and Drive Systems*. New York, NY, USA: Wiley, 2002.

[19] M. Krstić and H.-H. Wang, "Stability of extremum seeking feedback for general nonlinear dynamic systems," *Automatica*, vol. 36, no. 4, pp. 595–601, 2000.

[20] V. Kumar, R. R. Joshi, and R. C. Bansal, "Optimal control of matrix-converter-based WECS for performance enhancement and efficiency optimization," *IEEE Trans. Energy Convers.*, vol. 24, no. 1, pp. 264–273, Mar. 2009.

[21] A. D. Luca and G. Ulivi, "Dynamic decoupling of voltage frequency controlled induction motors," in *Proc. 8th Int. Conf Anal. Optim. Syst.*, 1988, pp. 127–137.

[22] A. D. Luca and G. Ulivi, "Design of exact nonlinear controller for induction motors," *IEEE Trans. Autom. Control*, vol. 34, no. 12, pp. 1304–1307, Dec. 1989.

[23] L. Luo and E. Schuster, "Mixing enhancement in 2D magnetohydrodynamic channel flow by extremum seeking boundary control," in *Proc. Amer. Control Conf.*, 2009, pp. 1530–1535.

[24] R. Marino, S. Peresada, and P. Valigi, "Adaptive input-otput linearizing control of induction motors," *IEEE Trans. Autom. Control*, vol. 38, no. 2, pp. 208–221, Feb. 1993.

[25] B. Ozpineci and L. M. Tolbert, "Simulink implementation of induction machine model—A modular approach," in *Proc. IEEE Int. Conf. Electr. Mach. Drives*, Feb. 2003, pp. 728–734.

[26] T. Pan, Z. Ji, and Z. Jiang, "Maximum power point tracking of wind energy conversion systems based on sliding mode extremum seeking control," in *Proc. IEEE Energy Conf.*, Nov. 2008, pp. 1–5.

[27] L. Y. Pao and K. E. Johnson, "Control of wind turbines," *IEEE Control Syst. Mag.*, vol. 31, no. 1, pp. 44–62, Feb. 2011.

[28] T. Senjyu, R. Sakamoto, N. Urasaki, T. Funabashi, H. Fujita, and H. Sekine, "Output power leveling of wind turbine generator for all operating regions by pitch angle control," *IEEE Trans. Energy Convers.*, vol. 21, no. 2, pp. 467–475, Jun. 2006.

[29] J. G. Slootweg, S. W. H. de Haan, H. Polinder, and W. L. Kling, "General model for representing variable speed wind turbines in power system dynamics simulations," *IEEE Trans. Power Syst.*, vol. 18, no. 1, pp. 144–151, Feb. 2003.

[30] M. S. Stankovic, K. H. Johansson, and D. M. Stipanovic, "Distributed seeking of nash equilibria with applications to mobile sensor networks," *IEEE Trans. Autom. Control*, vol. 57, no. 4, pp. 904–919, Apr. 2012.

[31] M. S. Stankovic and D. M. Stipanovic, "Extremum seeking under stochastic noise and applications to mobile sensors," *Automatica*, vol. 46, no. 8, pp. 1243–1251, Aug. 2010.

[32] Y. Tan, D. Nešić, and I. Mareels, "On non-local stability properties of extremum seeking control," *Automatica*, vol. 42, pp. 889–903, Jun. 2006.

[33] A. R. Teel and D. Popovic, "Solving smooth and nonsmoooth multivariable extremum seeking problems by the methods of nonlinear programming," in *Proc. Amer. Control Conf.*, 2001, pp. 2394–2399.
[34] H.-H. Wang, S. Yeung, and M. Krstić, "Experimental application of extremum seeking on an axial-flow compressor," *IEEE Trans. Control Syst. Technol.*, vol. 8, no. 2, pp. 300–309, Mar. 2000.
[35] P. W. Wheeler, J. Rodriguez, J. C. Clare, L. Empringham, and A. Weinstein, "Matrix converters: A technology review," *IEEE Trans. Ind. Electron.*, vol. 49, no. 2, pp. 276–288, Apr. 2002.
[36] B. Wu, Y. Lang, N. Zargari, and S. Kouro, *Power Conversion and Control of Wind Energy Systems*. New York, NY, USA: Wiley, 2011.
[37] S. Zhang, K. J. Tseng, and T. D. Nguyen, "Modeling of AC-AC matrix converter for wind energy conversion system," in *Proc. IEEE Conf. Ind. Electron. Appl.*, May 2009, pp. 184–191.

Azad Ghaffari received the B.S. degree in electrical engineering and the M.S. degree in control engineering from the K. N. Toosi University of Technology, Tehran, Iran, and the Ph.D. degree in mechanical and aerospace engineering from the Joint Doctoral Program between San Diego State University and the University of California, San Diego, CA, USA.

His current research interests include demand response in power systems, extremum seeking and its application to maximum power point tracking in photovoltaic and wind energy conversion systems, induction machines, power electronics, and sliding mode control.

Miroslav Krstić (F'01) received the Dipl.Ing. degree in electrical engineering from the University of Belgrade, Belgrade, Serbia, and the M.S. and Ph.D. degrees in electrical engineering from the University of California, Santa Barbara, CA, USA, in 1989, 1992 and 1994, respectively.

He holds the Daniel L. Alspach Endowed Chair and is the Founding Director of the Cymer Center for Control Systems and Dynamics, University of California San Diego (UCSD), San Diego, CA, USA. He serves as an Associate Vice Chancellor for Research with UCSD. He has co-authored ten books on adaptive, nonlinear, stochastic control, extremum seeking, and control of partial differential equations systems, including turbulent flows and control of delay systems.

Dr. Krstić is a fellow of the International Federation of Automatic Control. He has held the Russell Severance Springer Distinguished Visiting Professorship with UC Berkeley, Berkeley, CA, USA, and the Royal Academy of Engineering Distinguished Visiting Professorship. He serves as a Senior Editor for the IEEE TRANSACTIONS ON AUTOMATIC CONTROL and *Automatica*, an Editor of two Springer book series, a Vice President for Technical Activities of the IEEE Control Systems Society (CSS), and a Chair of the IEEE CSS Fellow Committee. He received the Presidential Early Career Award for Scientists and Engineers, the National Science Foundation Career Award, the Office of Naval Research Young Investigator Award, the Axelby and Schuck Paper Prizes Award, and the first UCSD Research Award from engineering.

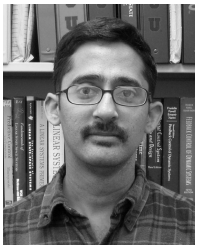

Sridhar Seshagiri received the B.Tech. degree in electrical engineering from IIT Madras, Chennai, India, and the M.S. and Ph.D. degrees in electrical engineering from Michigan State University, East Lansing, MI, USA, in 1995, 1998, and 2003 respectively.

He joined the Department of Electrical and Computer Engineering, San Diego State University, San Diego, CA, USA, in 2003, where he is currently an Associate Professor. His current research interests include nonlinear control with applications to energy systems, in particular control of power electronic converters.